Hemodynamics of the sternocleidomastoid measured with frequency domain near-infrared spectroscopy towards non-invasive monitoring during mechanical ventilation

RAEEF ISTFAN,[1] CARLOS A. GÓMEZ,[1] MATTHEW APPLEGATE,[1] DMITRY ROZENBERG,[2] W. DARLENE REID,[3,4,5] AND DARREN ROBLYER[1,*]

[1] *Department of Biomedical Engineering, Boston University, Boston, MA 02125, USA*
[2] *Department of Medicine, Respirology and Lung Transplantation, University Health Network, University of Toronto, Toronto, ON, Canada*
[3] *Department of Physical Therapy, University of Toronto, Toronto ON, Canada*
[4] *Interdepartmental Division of Critical Care Medicine, University of Toronto, Toronto, ON, Canada*
[5] *KITE - Toronto Rehabilitation Institute, University Health Network, Toronto, ON, Canada*
[*]roblyer@bu.edu

Abstract: Mechanical ventilation (MV) is used to assist spontaneous breathing in critically ill patients in the intensive care unit (ICU). MV is a cornerstone of critical care medicine but it is now known that inspiratory muscle dysfunction due to injury, disuse, and/or atrophy during MV plays a major role in outcomes for these patients. For example, prolonged MV is strongly correlated with dysfunction of the sternocleidomastoid (SCM), an accessory inspiratory muscle that has been linked to weaning failure from MV. Hemodynamic monitoring of the SCM may provide an important non-invasive and real-time means to monitor MV. In this work, we first conducted multi-layer Monte Carlo simulations to confirm the ability of near infrared light to detect changes in the oxygenation of the SCM over wide ranges of skin tones and adipose layer thicknesses. We then optimized a custom digital frequency domain near-infrared spectroscopy (FD-NIRS) system for continuous 10 Hz measurements of the SCM at 730 nm and 850 nm. A healthy volunteer study was conducted (N=10); subjects performed sets of isometric neck flexions of the SCM. Substantial changes in oxyhemoglobin + oxymyoglobin (oxy[Hb + Mb]), deoxyhemoglobin + deoxymyoglobin (deoxy[Hb + Mb]), and total hemoglobin + myoglobin (total[Hb + Mb]) were observed during sustained and intermittent isometric flexions. There were notable sex differences observed in the magnitude of hemodynamic changes (~2x larger changes in males for oxy[Hb + Mb] and deoxy[Hb + Mb]). The magnitude of hemodynamic changes when taking into account μ_s' changes during flexions was ~ 2-2.5x larger as compared to assuming constant scattering (CS), which is a common assumption used for continuous wave (CW) NIRS methods. This study suggests that FD-NIRS provides improved accuracy for hemodynamic monitoring of the SCM compared to CW-NIRS, and that FD-NIRS may provide value for SCM monitoring during MV.

1. Introduction

Critically ill patients requiring mechanical ventilation (MV), which is used to assist breathing, incurred an estimated $27 billion in expenditures in the US in 2010, accounting for 12% of all hospital costs [1]. In that same year there were 2.7 episodes of MV per 1000 population, highlighting the enormous importance of this procedure [1]. The COVID-19 pandemic has substantially increased these numbers, although precise rates are not yet available [2]. MV is a cornerstone of critical care medicine [3], but intensive care unit (ICU) stays greater than

7 days and older age are currently the best predictors of profound long-term cognitive and physical disability related to MV [4]. A key part of this problem stems from the fact that approximately 30-40% of critically ill patients in the ICU have difficulties being weaned from MV, accounting for ~40% of total ICU costs, and increased morbidity and mortality [4–6]. It is now known that inspiratory muscle dysfunction due to injury, disuse, and/or atrophy during MV plays a major role in outcomes for these patients. For example, prolonged MV is strongly correlated with dysfunction of primary (e.g. diaphragm) and accessory inspiratory muscles (e.g. sternocleidomastoid (SCM)); both have been linked to weaning failure [7–9]. Weaning failure can be defined as the inability to breathe spontaneously when removed from mechanical ventilation within 48 hours to seven days after assisted ventilation was instituted [10]. More generally, longer ICU length of stay is in part attributable to respiratory muscle dysfunction [7,11] and inspiratory muscle dysfunction are associated with ICU readmission [5].

MV is used, in part, to "unload", or reduce the metabolic effort of respiratory muscles in order to redirect oxygen delivery to vital organs. As the patients' conditions improve, key inspiratory muscles (e.g. diaphragm, scalenes, SCM, etc.) need to take over spontaneous breathing independent of the ventilator. This "reloading" is precarious due to muscle disuse atrophy, induced by unloading, compounded by oxidative stress and inflammation that accentuates their dysfunction [9,12]. This is further complicated by other common conditions in the ICU, such as septic or cardiogenic shock, which can severely limit oxygen delivery independent of muscle status [13,14]. Currently, there are no reliable means of establishing whether the inspiratory muscles are adequately or excessively unloaded when setting MV parameters.

Hemodynamic monitoring of the SCM may provide an important non-invasive and real-time means to monitor MV. The SCM is a muscle located in the neck connecting the mastoid process to the clavicle and manubrium, and its contraction can turn and/or flex the head forward. It is also an accessory muscle of inspiration that is recruited during higher levels of ventilation that occurs during exertion. Moreover, the SCM is recruited more often during spontaneous breathing trials when patients fail to wean [15]. Previous studies have shown that significant changes in oxygenation occur in the SCM during inspiratory threshold loading tests, which simulate distressed breathing [16]. Several prior works have used continuous wave near-infrared spectroscopy (CW-NIRS) techniques to measure relative changes in oxygenation of various inspiratory muscles including the SCM [16–21]. While CW systems are able to detect changes in oxygenation, they cannot extract absolute tissue optical properties or chromophore concentrations without the use of explicit assumptions such as an assumed differential pathlength factor (DPF, the ratio between the mean optical pathlength and the source detector separation [22,23]). This potentially leads to errors in estimates of muscle metabolic changes due to incorrect assumptions about tissue scattering [24,25].

Frequency domain near-infrared spectroscopy (FD-NIRS), also called frequency domain diffuse optical spectroscopy (FD-DOS), uses temporally modulated light at MHz frequencies to illuminate a tissue volume. The measured changes in amplitude and phase of the remitted light are used to calculate the tissue optical absorption coefficient (μ_a) and the reduced scattering coefficient (μ_s') [26]. When performed at multiple carefully chosen wavelengths, this method allows for the extraction of absolute concentrations of chromophores such as oxy and deoxyhemoglobin. FD-NIRS/FD-DOS has been previously used for breast cancer chemotherapy treatment monitoring [27–29] and monitoring the hemodynamics of the brain [30]. There has also been prior work using FD-NIRS to measure the oxygenation of various muscles in the limbs and chest [31,32], but to the best of our knowledge, FD-NIRS has not been used to monitor the SCM.

In this work, we first describe results from Monte Carlo simulations demonstrating that NIR light is sensitive to anticipated hemodynamic changes in the SCM. We then describe how our custom digital FD-NIRS measurement platform was adapted to provide two-wavelength high-SNR measurements of the SCM with a rapid data processing pipeline. We then describe the

results of a healthy volunteer study in which subjects performed two different quasi-isometric neck flexions while monitored with FD-NIRS. Finally, we describe how FD and CS analyses of the same data set lead to different hemodynamic results, and describe the implications of this study for future work.

2. Methods

2.1. Monte Carlo simulations

A multilayer model of the neck was created using Monte Carlo eXtreme (MCX), a Monte Carlo based photon transport simulator, in order to confirm that light from our FD-NIRS system can adequately probe the SCM [33]. For these simulations, a pencil beam source pointing in the +z direction was used, and 6 different detectors, each with a 2 mm diameter, were placed 10-35 mm away from the source. Internal reflections of photons between the layers were included, but not external reflections (photons can escape). The simplified multi-layer model is shown in Fig. 1. The optical properties used for each layer in the simulation were estimated by using average properties found in the literature and are shown in Table 1 [34–43]. The SCM lies below two superficial layers: the skin containing the epidermis and the dermis which is typically 1-2 mm thick [44]; and the subcutaneous fat layer with a thickness that varies from person to person. The SCM itself is approximately 5 mm thick on average [45]. The tissue below the SCM contains connective tissue and other tissue types, which we simply refer to as "deep tissue". Finally, the internal jugular vein (IJV) and the common carotid artery (CA) are deep to some parts of the SCM. Using prior work as well as our own ultrasound images, the IJV was modeled as a 5 mm radius cylinder directly below the SCM and the CA was modeled as a 3.5 mm radius cylinder 3.5 mm below the SCM [46].These vessels contain a high concentration of blood, which is extremely absorbing relative to the surrounding tissue. The main absorbers of light in the near infrared wavelengths are water, lipids, hemoglobin in blood vessels, and myoglobin found in muscle cells. Since hemoglobin and myoglobin have very similar optical spectra in this wavelength range, they are difficult to separate optically and their combined concentrations will be presented as [Hb+Mb] [47].

Table 1. The optical properties used for the Monte Carlo simulations at baseline. Three different optical properties were used for skin labeled skin 1 (lightest, white) to skin 3 (darkest, black). For the simulations that did not involve varying skin absorption, skin 2 optical properties were used. g is the anisotropy factor and n is the index of refraction. SubQ refers to subcutaneous.

Layer	μ_a (mm^{-1})		μ_s' (mm^{-1})		g		n	References
	730 nm	850 nm	730 nm	850 nm	730 nm	850 nm		
Skin 1	0.018	0.015	2.69	2.16	0.83	0.87	1.40	[34–37,39]
Skin 2	0.046	0.038	2.69	2.16	0.83	0.87	1.40	[34,35,37,39,40]
Skin 3	0.125	0.060	2.69	2.16	0.83	0.87	1.40	[34–37,39]
Fat (SubQ)	0.010	0.010	1.43	1.29	0.75	0.75	1.44	[35,36,41,42]
SCM	0.024	0.031	0.56	0.42	0.90	0.90	1.37	[35,36,38,42]
Deep Tissue	0.010	0.010	1.17	0.97	0.90	0.90	1.40	[35]
IJV	0.387	0.543	1.55	1.24	0.98	0.98	1.39	[43]
CA	0.258	0.607	1.61	1.29	0.98	0.98	1.39	[43]

The oxygen saturation (StO_2) and [Hb+Mb] of the muscle layer was varied in simulation in order to determine the optical sensitivity to hemodynamic changes in the SCM. The baseline total hemoglobin + myoglobin concentration (total[Hb+Mb]) was determined using Beer's Law by scaling previously reported muscle optical absorption values by the extinction spectrum of deoxyhemoglobin [36,48]. This was done after subtracting the absorption due to water (assumed
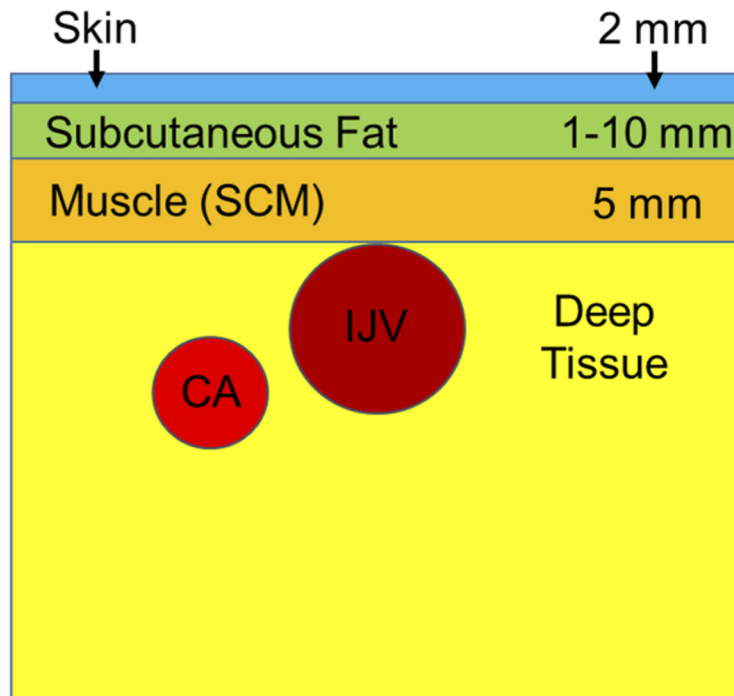
Fig. 1. The geometry of the neck used for the Monte Carlo simulations. The subcutaneous fat layer thickness was varied from 1- 10 mm and 3 different skin absorptions were used to simulate a variety of skin tones. The optical properties of the SCM were varied to simulate the effects of two different hemodynamic perturbations.

to be 62.5%) [39,49–51]. The resulting baseline total[Hb+Mb] was 129 μM. The StO_2 at baseline was estimated to be 70%. The optical properties of the muscle layer were changed by varying both the total[Hb+Mb] as well as the StO_2.

We simulated two different perturbations and resulting hemodynamic changes previously described in the literature: 1) task failure during a neck flexion, which increased total[Hb+Mb] by 9.0 μM and decreased StO_2 by 2.03%, and 2) task failure during an inspiratory threshold loading test, which increased total[Hb+Mb] by 20.7 μM and decreased StO_2 by 8.00% [16]. Task failure for both tasks is defined as the moment when the subject is unable to perform the task at the proper difficulty for the third consecutive time. We then calculated the difference in detected light between baseline and the two perturbations by simulating 10^9 photon packets in the Monte Carlo simulation for each scenario. The simulation outputs included the pathlength of each detected photon packet for each layer, which when weighted by the absorption coefficient (μ_a) in each layer gave the resulting detected photon weight. The overall sensitivity to the SCM was calculated by comparing the total detected photon weight of the different scenarios at 6 different source detector (SD) separations from 10-35 mm. We also investigated the effects of lipid layer thickness by varying the lipid layer from 1-10 mm and skin absorption by comparing the effects of 3 different skin absorption values found in the literature corresponding to range of skin tones [15,19].

2.2. Custom FD-NIRS system

We adapted our previous custom digital FD-NIRS system to take SCM measurements on the neck. A system block diagram is shown in Fig. 2 and prior versions of this system are described in

more detail elsewhere [52–54]. Briefly, direct digital synthesizers (DDS) were used to modulate two fiber coupled laser diodes at 730 and 850 nm (Blue Sky FMXL730-030YFGA, ThorLabs LP852-SF30). The lasers were modulated at 145/155 MHz respectively to allow temporal multiplexing. The detected light was measured by a fiber coupled avalanche photodiode (APD) (Hamamatsu S11519-30). The resulting signal was digitized by a 250 MHz analog to digital converter (ADC), where it was compared to a reference signal picked off from the DDS chips to determine the changes in amplitude and phase induced by the tissue. A calibration procedure was used to remove the instrument response function as previously described [53]. Amplitude and phase were computed in an field-programmable gate array (FPGA) using the Goertzel Algorithm [33,34].
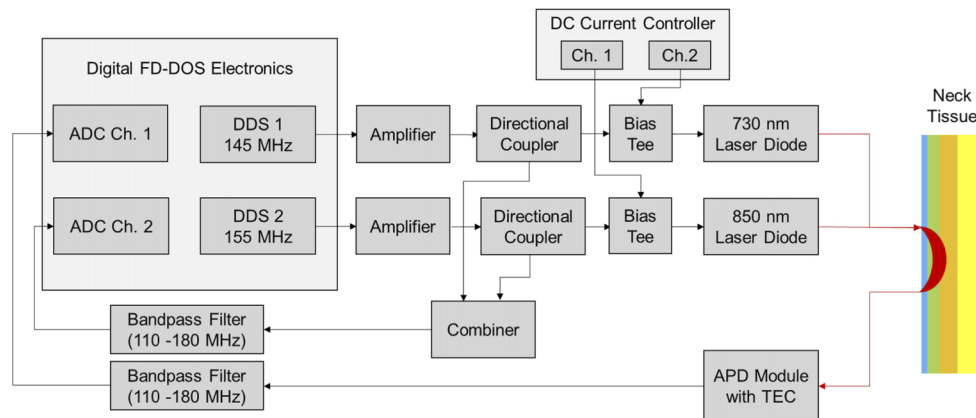

Fig. 2. The system block diagram for our custom digital FD-NIRS system adapted for SCM measurements. DDS = Direct Digital Synthesizer, ADC = Analog to Digital Converter, APD = Avalanche Photodiode, TEC = Thermoelectric Cooler.

A number of parameters for the system were adapted in order to optimize the system for SCM measurements. Most importantly, the SCM is generally more absorbing than tissue that has been measured previously by our system (e.g. breast, finger, forearm [53–55]), and so the system was optimized for maximum signal to noise ratio (SNR) while maintaining measurement speeds of at least 10 Hz, a rate commonly used by previous CW studies of the SCM [14–15]. The two wavelengths used here, 730 nm and 850 nm, were chosen for their ability to separate oxy[Hb+Mb] and deoxy[Hb+Mb] as they are on different sides of hemoglobin's isosbestic point. Additionally, high SNR was achieved for the lasers at these wavelengths. We did not add additional lasers as each laser would need to be operated at lower power due to ANSI limits. The source and detector fibers were placed 25 mm away from each other, the largest source-detector separation that gave an adequate SNR through the SCM based on feasibility data. The DDS signal was amplified (11 dB and 1 dB for 730 nm and 850 nm respectively) to increase RF power to the lasers and to maximize the modulation depths of the lasers while avoiding clipping. A 110-180 MHz Bandpass filter was used to reduce background noise in the detected signal. Measurements were captured using 65536 digital samples/modulation frequency, and 36 repetitions were averaged, resulting in an overall measurement rate of 10 Hz. The system SNR measured on a silicone optical phantom with similar optical properties to neck tissue ($\mu_a = 0.034, 0.017$ mm^{-1} and $\mu_s' = 0.51, 0.50$ mm^{-1} at 730, 850 nm) was 42.0 dB and 42.3 dB for 730 nm and 850 nm respectively. Both lasers diodes were fiber coupled to 400-μm core diameter fibers bundled into a single ferrule to deliver light to the tissue. A 2.3-mm core diameter fiber bundle was used to collect remitted light. Both fibers were custom made by Fiberoptic System Inc. (Simi Valley, CA) and terminated at a right angle

so they could lie flat against the neck. A custom fiber holder was 3D printed to hold the right angle source and detector fibers on the tissue.

2.3.   Healthy volunteer study

FD-NIRS measurements were conducted on a group of healthy volunteers (N=10) in order to confirm the ability to measure changes in the SCM. The group of volunteers consisted of 5 males and 5 females, aged 26-38 years old with the following ethnicities: Caucasian n=8, South Asian n=1, Asian n=1. All measurements were conducted under an institutionally approved protocol (BU IRB 5618E). The exclusion criteria included anyone who was considered high risk for COVID-19. All participants were informed about the study virtually before consenting in person and subjected to the appropriate COVID-19 safety protocols.

Hemodynamic changes of the SCM were induced by performing a series of quasi-isometric neck flexions previously shown to affect the hemodynamics of the SCM [56]. The measurement setup is shown in Fig. 3. Each volunteer was seated upright with the neck and head in a neutral position against a headrest and their forehead strapped to a force sensor (Shimpo FG-3009).The probe containing the source and detector fibers was placed on the skin above the SCM midway between its origin (manubrium and clavicle) and insertion (mastoid process) and secured using Tegaderm tape. Initially, the participant performed a maximum voluntary contraction (MVC), followed by a 30-second sustained contraction, a 3 minute rest, and lastly, intermittent contractions. The latter of which was considered to parallel intermittent contractions performed during inspiration. Participants were able to target contractions to a specific percentage of MVC by visualizing the indicated level on a computer monitor. The 30 second sustained flexion was performed by targeting 75% of their MVC whereas the intermittent flexions were performed with a duty cycle of 3 sec contraction to 3 sec relaxation and an intensity of 60% MVC for a 10 minute duration or until task failure. Task failure was defined as the point when the volunteer could no longer reach their target force for 3 consecutive contractions. Additionally, after the conclusion of the FD-NIRS measurements, each subject's skin + lipid layer thickness was measured using ultrasound (Vscan, General Electric) at the FD-NIRS measurement location. The skin + lipid layer thickness was measured from the surface to a clearly defined region between the lipid layer and the muscle. The average of muscle depth measurements taken at the left and right hand sides of the image were used to calculate the skin+lipid layer thickness.

2.4.   Signal processing and data analysis

An inverse model which utilized a Monte Carlo based Lookup Table (LUT) was used to calculate μ_a and μ_s' in post processing for FD data. The method is similar to an analytical model based LUT inverse model described in our previous work [57]. First, a series of white (i.e. zero absorption) Monte Carlo simulations were performed with μ_s' ranging from 0.1 to 2.0 mm^{-1} in increments of 0.1 mm^{-1} using a pencil beam source and a detector that matched the diameter and numerical aperture (NA) of the experimentally used detector fiber. The arrival times of photon packets were binned in 10 ps intervals to generate the temporal point spread function (TPSF) for each value of μ_s'. A TPSF for arbitrary values of μ_s' could then be estimated by linearly interpolating the TPSFs of two simulations spanning the desired μ_s' values. The final TPSF, including absorption, was constructed by scaling each bin of the TPSF using Beer's law. Amplitude and phase changes induced by the tissue were then calculated by Fourier transforming the TPSF [58,59]. This Monte Carlo based forward model was used to calculate the amplitude and phase for a dense grid of μ_a and μ_s' pairs to form a LUT. Experimental data were compared with each element of the LUT and the nearest optical property pair was used as the value associated with the tissue [60]. This LUT method was validated by measuring a set of 13 silicone optical phantoms with optical properties similar to the neck region, and compared the resulting μ_a and μ_s' to a traditional analytical model [26]. The percent difference between these two
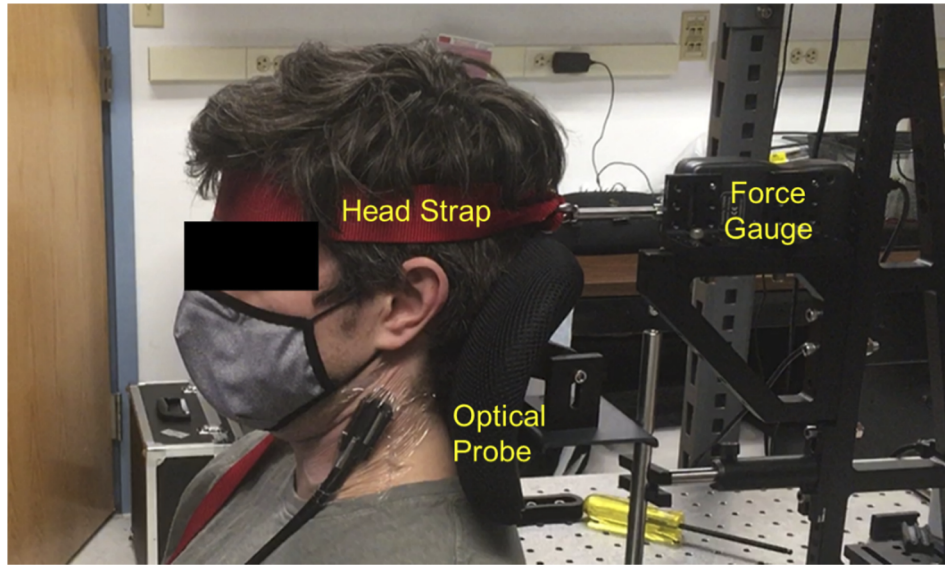
Fig. 3. The system setup for the healthy volunteer study. The subjects performed quasi-isometric neck flexions by pushing their forehead forwards against the head strap. A force gauge was used to measure the applied force, which was projected on a monitor in front of them.

methods was 4.8% in μ_a and 5.7% in μ_s' across this set of phantoms (Figure S2). Beer's Law was used to calculate concentrations of oxyhemoglobin + oxymyoglobin (oxy[Hb + Mb]) and deoxyhemoglobin + deoxymyoglobin (deoxy[Hb + Mb]). A 20% lipid fraction and 62.5% water fraction were assumed for the entire tissue [35,39,49–51]. At these wavelengths, water and lipid account for only a small, but measurable fraction (5-10%) of the total absorption, with the absorption due to water being an order of magnitude higher than the absorption due to lipids.

For the sustained flexions, a first order linear locally weighted scatterplot smoothing (LOWESS) filter with a 20 point (2 s) window was used in order to smooth the data. Differences in the chromophores were calculated between the onset of the flexion and maximum changes during the flexion (local maximum for deoxy[Hb + Mb] and total[Hb + Mb] and a local minimum for oxy[Hb + Mb]). Maximal points were manually selected to avoid obvious artifacts due to motion. For the intermittent flexions, a first order linear LOWESS filter with a 600 point (60 s) window was used in order to smooth the data to calculate the trend of the resulting signal while averaging the oscillations that occurred every 3 seconds while the subjects are contracting and relaxing their SCM. Oxy[Hb + Mb], deoxy[Hb + Mb], and total[Hb + Mb] were selected at three different timepoints: the onset of the flexion, the maximum of the early changes (defined as < 3 min after the onset of the flexion), and the end of flexion after 10 mins or at task failure. The differences between the baseline and maximum early and late changes were also calculated. Mann-Whitney U Tests were used to compute the statistical significance of the resulting chromophore changes between males and females as well as between FD and constant scattering (significance level $p<0.05$). All data analysis and signal processing was performed using MATLAB (Mathworks, Natick, MA).

Amplitude data was also analyzed using the modified Beer-Lambert Law (Eq. (1)) in order to compare FD results in which continuously updated μ_s' measurements are available, against a constant scattering (CS) scenario, which is often used with CW-NIRS analysis in muscle measurements studies [16]. An estimate for DPF is required in order to calculate the change in μ_a using this method. The DPF represents the ratio between the mean optical pathlength and the

source-detector separation. The DPF accounts for multiple scattering events that occur in tissue, which increase photon pathlength compared to the source-detector separation [22,23]. For the CS scenario, a DPF of 4 was used similar to prior work [16]. Additionally, the first μ_a measurement for each experiment was used to obtain an estimate for the baseline values of the chromophores, and the modified Beer-Lambert Law was used to calculate changes in μ_a assuming a constant DPF of 4 throughout the experiment. Equations (1) and (2) were used to calculate $\Delta\mu_a$ as well as the DPF when it wasn't fixed. In these equations, d represents the source-detector separation (25 mm for this work).

$$\Delta\mu_a(\lambda) = \frac{1}{DPF(\lambda) * d} * ln\left(\frac{amp(\lambda, 0)}{amp(\lambda, t)}\right) \tag{1}$$

$$DPF(\lambda) = \frac{1}{2}\sqrt{\frac{3\mu_s'(\lambda)}{\mu_a(\lambda)}}\left[1 - \frac{1}{\left(1 + d\sqrt{3\mu_a(\lambda)\mu_s'(\lambda)}\right)}\right] \tag{2}$$

3. Results

3.1. Monte Carlo simulation results

The two different simulated perturbations: neck flexions and an inspiratory threshold loading challenge, both resulted in a decrease of detected light at both wavelengths. A larger decrease was observed at 730 nm compared to 850 nm due to the decrease in StO_2. Figure 4 shows the relative sensitivity of the SCM to the simulated inspiratory threshold loading challenge at six source-detector separations (10-35 mm) and 10 lipid layer thicknesses (1-10 mm). In general, the sensitivity to the SCM increased as the source-detector separation increased, with longer source detector separations being more sensitive to hemodynamic changes in the SCM.
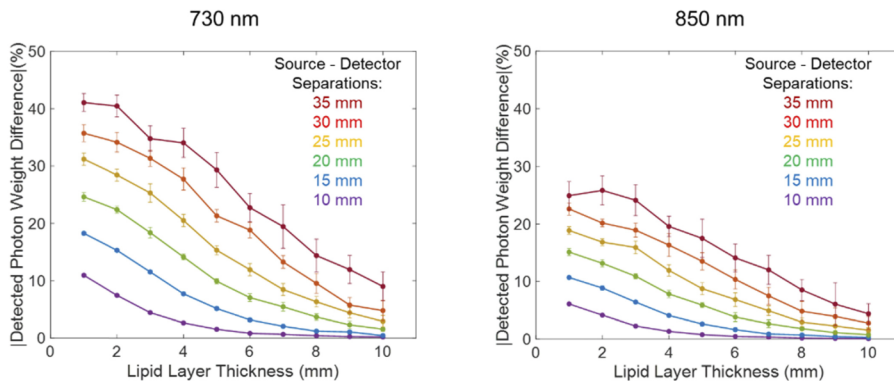

Fig. 4. The sensitivity to a hemodynamic change in the SCM simulating an inspiratory threshold loading challenge. The simulations were run at 10 different lipid layer thicknesses (1-10 mm) and 6 different source detector separations (10-35 mm). The error bars represent the standard deviation of 10 simulations.

In general, sensitivity to the SCM decreased as the lipid layer thickness increases. Previous groups have excluded subjects with a lipid layer great than 10 mm citing a lack of SCM measurement sensitivity under those conditions [16]. These simulation results support this finding, especially for short source detector separations. The sensitivity to the perturbations were similar for the three skin absorptions tested, resulting in a less than a 3.0% difference between the 3 pairs of absorptions. However, it is important to note that the amount of detected light decreases as the skin gets darker and more absorbing, resulting in lower detected photon weights

and lower measurement SNR, which could make it more challenging to measure these individuals. Blood oxygenation changes of the IJV and internal CA were also tested to determine if these large vessels could affect measurements of the SCM. We found that oxygenation changes in these vessels had a minimal effect on the detected signal (<10%) for the SD separations tested and the geometry used here.

Based on these results, as well as the feasibility measurements described earlier, a SD separation of 25 mm was chosen for healthy volunteer measurements. This SD separation should provide substantial sensitivity to changes in expected SCM hemodynamics regardless of skin tone and for a wide range of adipose thicknesses.

3.2. Healthy volunteer study

At baseline, the average oxy[Hb + Mb] was 104.7 ± 36.3 μM, deoxy[Hb + Mb] was 56.6 ± 11.8 μM and total[Hb + Mb] was 161.4 ± 43.6 μM. Additionally baseline optical properties are shown in Table S1. Large changes in the hemodynamics of the SCM were observed during flexions. Figure 5 shows changes in deoxy[Hb + Mb], oxy[Hb + Mb] and total[Hb + Mb] in a set of sample flexions. Figure 6 shows a summary of the observed changes across the group of volunteers.
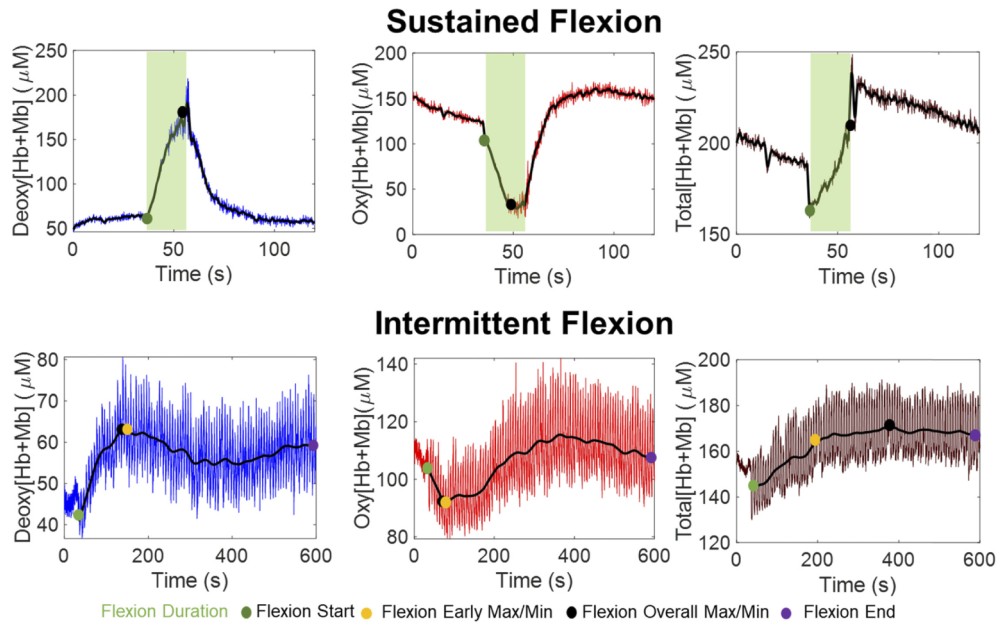

Fig. 5. Sample chromophore data from the sustained flexions (top) and the intermittent flexions (bottom). The black line indicates the smoothed data. The colored points indicate the points of interest: the beginning of the flexion, the early maximum/minimum, and the end of the flexion.

For the sustained 30 second flexion, the majority of the subjects had an increase in deoxy[Hb + Mb], a decrease in oxy[Hb + Mb], and an initial decrease followed by an increase in total[Hb + Mb]. The maximal change for these parameters typically occurred close to the end of the flexion. There was one subject that had an increase in oxy[Hb + Mb] during the flexion (rather than the more common decrease).

For the longer 10-minute intermittent flexion, there was typically a distinct early phase of hemodynamic changes that occurred within the first three minutes, followed by slower changes over the remainder of the measurement. The early changes typically presented as rapid increases in deoxy[Hb + Mb] and decreases in oxy[Hb + Mb]. The increases observed in total[Hb + Mb] are
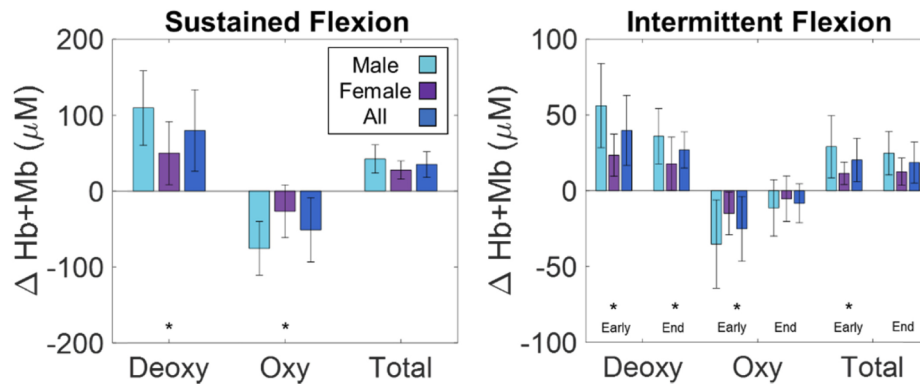
Fig. 6. Summarized FD-NIRS results from the healthy volunteer study. The bars indicate the mean and the error bars indicate the standard deviation of the group or subset of volunteers. The asterisk indicates that the male and female values are significantly different using a Mann-Whitney U Test (p < 0.05).

more complicated and followed one of two distinct patterns (see Figure S2). In some subjects, the changes occurred in a sustained manner over the duration of the intermittent contraction whereas in others, total[Hb + Mb] reached a maximum during the early phase, similar to deoxy[Hb+Mb], followed by a gradual decrease. By the end of the intermittent flexion, deoxy[Hb + Mb] was typically higher than baseline and oxy[Hb + Mb] was typically lower than baseline, but to a lesser extent than at the early phase of the measurement. Total[Hb+Mb] typically ended higher than baseline.

Figure 6 also highlights the differences in the magnitude of the hemodynamic changes between males and females. The absolute changes for deoxy[Hb + Mb], oxy[Hb + Mb], and total[Hb + Mb] were approximately 2-2.5x larger in males compared to females for both sustained flexion and both early at later time points of the intermittent flexions. Statistical significance was observed in 6 out the 9 comparisons as indicated in the figure.

3.3. Comparison between FD and CS analyses

Figure 7 shows an example of amplitude, phase, μ_a and μ_s' changes during a sustained flexion. Tables S1 shows average changes in these parameters over all of the study subjects. In general, there were changes in both amplitude and phase, as well as μ_a and μ_s' during flexions. There were several notable differences when comparing FD and CS analyses of chromophore changes. An example of this is shown in Fig. 7 (rightmost column), and the study averages are shown in Fig. 8. FD analyses yielded magnitude of changes that were ~ 2-2.5x larger on average compared to CS analyses. These differences may be due in part to the observed changes in μ_s' during the flexions, which are not accounted for in the CS method, which assumes a constant DPF throughout the measurement. It is also of note that the DPF calculated using baseline FD-derived μ_a and μ_s' values was 3.28 ± 0.50 at 730 nm and 2.77 ± 0.61 at 850 nm across the study subjects. These both differ from the assumed DPF of 4 used for CS processing [16,17]. During the sustained flexion the DPF decreased by 0.70 ± 0.26 at 730 nm and 0.19 ± 0.39 at 850 nm. It is also of note that the FD-derived chromophores were noisier than the CW-derived chromophores. This appears to be related to the inclusion of phase measurements in the FD analysis, which were substantially noisier than the amplitude data.
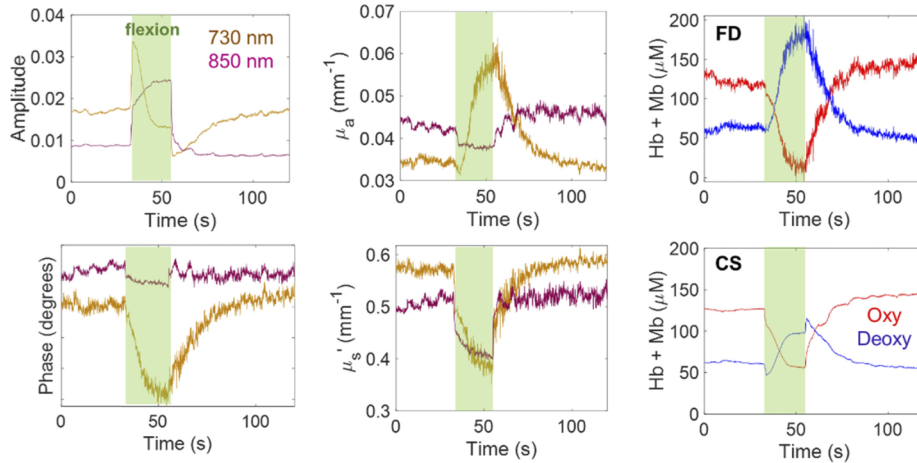
Fig. 7. Sample amplitude, phase, μ_a and $\mu_s{}'$, and chromophore data from a sustained flexion. The rightmost column shows chromophore processed with FD (top) and CW (bottom).
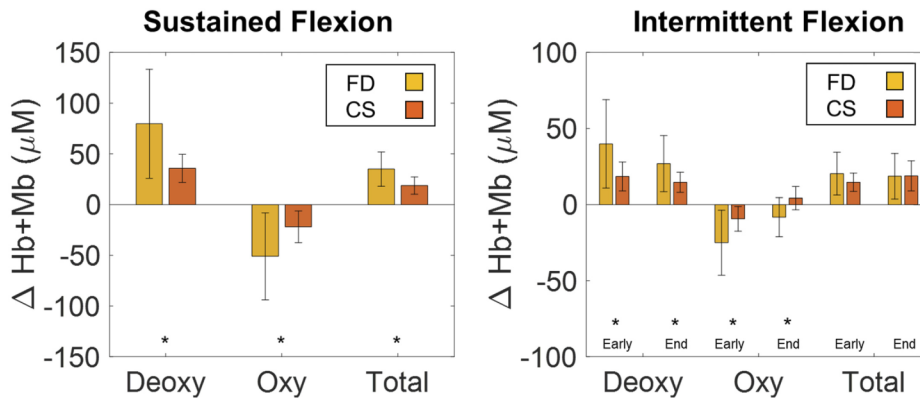

Fig. 8. Summarized results from the healthy volunteer study comparing FD-NIRS analysis to constant scattering (CS) analysis. The bars indicate the mean and the error bars indicate the standard deviation of the group of volunteers. The asterisk indicates that the FD and CS values are significantly different using a Mann-Whitney U Test ($p < 0.05$).

4. Discussion

We have demonstrated here that quasi-isometric flexions of the SCM induce hemodynamic changes measurable with FD-NIRS. Changes included rapid drops in oxy[Hb + Mb] and increases in deoxy[Hb + Mb] and total [Hb + Mb]. On average, these changes were larger in male volunteers than female volunteers. Additionally, FD analyses led to chromophore changes that were consistently of larger magnitude compared to CS analyses. These results help to confirm that the additional information provided by FD-NIRS could give valuable insight into the physiology of the SCM while providing more accurate measurements compared with CW-NIRS.

The Monte Carlo simulation results confirmed that expected hemodynamic changes in the SCM induce large (>10%) changes in detected optical signals for SD separations of at least 25 mm. This was true up to about a 5 mm adipose layer thickness, after which changes decayed rapidly, especially for 850 nm. The average measured skin + adipose thickness for the volunteers in this study was 3.59 ± 0.74 mm, which strongly suggests that the FD-NIRS measurements of these volunteers were capable of detecting SCM hemodynamic changes. Skin tone had a relatively small effect on the relative detected signal changes in simulation, but darker skin decreased the overall detected signal amplitude substantially, which is an important factor when measuring a diverse patient population. The average optical properties measured from the healthy volunteers matched well to the optical properties of the muscle layer used in the MC simulations ($\mu_s' = 0.50 \pm 0.07$ mm^1 in volunteers vs 0.42 mm^{-1} in simulation for 850 nm). This serves as a validation that the optical properties used in the simulations were reasonable estimates for the measured tissue and is also a good indication that detected light traveled to the muscle layer. Since the top layers (skin and subcutaneous fat) have an approximate 2.5-5x higher μ_s' than the SCM layer, one would expect measured μ_s' to match these upper layers rather than the deeper SCM layer if there was insufficient measurement depth. We did not observe any statistically significant correlations between the measured adipose layer thicknesses and the magnitude of chromophores changes in volunteers. However, the measured volunteers were generally young (26-38 years old) and physically fit, and it is likely that inclusion of future subjects with thicker adipose layers may substantially attenuate measured SCM changes.

There were notable patterns in hemodynamic responses across subjects. For example, during the intermittent flexions, there was typically a substantial increase in deoxy[Hb + Mb] and a decrease in oxy[Hb + Mb] near the onset of the flexions. This is consistent with a rapid increase or overshoot in tissue oxygen extraction, which has been observed in prior works [47]. These changes are followed by a more gradual increase in total[Hb + Mb], consistent with prior work that indicates increased nitric oxide signaling to trigger vasodilation [47,61] enhancing oxygen delivery in response to increased oxygen consumption the muscle. It is also important to note that in some cases the measured tissue μ_s' values were less than 10x the μ_a values, which violates an assumption of the diffusion approximation [23]. For this reason, we opted to use a Monte Carlo based LUT to calculate the optical properties instead of a more traditional analytical model.

Large differences in the baseline chromophores as well as the magnitude of chromophore changes during flexions were observed between males and females. It has previously been observed that males, on average, have a higher hemoglobin content in blood measured from capillary and venous blood draws [62]. Our previous work using a similar FD-NIRS instrument has also observed large chromophore concentration difference between the sexes for bony anatomic locations [63]. Our work was limited by a small sample size whereas a larger sample size may provide more robust characterization of sex-differences. Regardless, these results strongly suggest that sex is an important factor to consider in future studies.

An advantage of FD-NIRS is the ability to quantify both μ_a and μ_s'. Conversely, CW-NIRS methods typically assume constant scattering and do not consider differences in optical properties at different wavelengths, inter-subject differences, or changes in μ_s' during dynamics. We observed μ_s' changes during flexions in this study of approximately 10.9% for 730 nm and 4.6%

for 850 nm. Other groups have also observed $\mu_s{}'$ changes during exercise in the forearms and the quadriceps [24,25]. Additionally, these prior studies also showed that $\mu_s{}'$ changes affected the resulting chromophores changes. However, unlike these previous studies, we observed larger changes in oxy[Hb+Mb] and deoxy[Hb+Mb] when using FD compared to CS during flexions, which was the opposite of what was previously reported. One possible explanation of this discrepancy is the relationship between the actual measured baseline optical properties (as measured with FD-NIRS) compared to the assumed DPF for CS analysis. While this study and the prior studies all assumed a DPF of 4 for the CS method, our subjects had a measured DPF at baseline of less than 4, while the prior studies had a measured DPF greater than 4. Following the modified Beer-Lambert Law, lower DPF values lead to larger $\Delta\mu_a$ changes and larger subsequent chromophore changes, potentially explaining why our FD data showed larger chromophore changes. Additionally, decreases in $\mu_s{}'$ were observed during many flexions, especially at 730 nm, which decreased the DPF even further and led towards larger chromophore changes. The results from prior work have been mixed, but generally show slight increases in scattering after exercise which was also attributed to an increase in total[Hb + Mb], which should lead to more red blood cells in the measured volume and potentially higher $\mu_s{}'$ [24] as well as the accumulation of metabolic by-products and hormones which could also increase $\mu_s{}'$ [24,25,64]. Therefore our decrease in scattering is surprising, given that we also saw an increase in total[Hb + Mb] during the same time period. Possible explanations for this discrepancy include changes in muscle configuration leading to changes in the partial volume probed by light, which mostly occurs during the onset of the flexion but can also occur during the flexion to a lesser extent. Additionally, deoxy[Hb] is slightly less scattering than oxy[Hb], which previous sources have noticed that it can in some cases counteract the increase in scattering due to the increases in total[Hb + Mb] if the decrease in saturation is significant enough [24,43,64]. It is also of note that the measured hemodynamic changes on healthy volunteers here were substantially larger than prior published CW measurements on the SCM [16]. For example, the average changes in total [Hb + Mb] were $18.6 \pm 15.0\ \mu M$ at the end of the intermittent flexions in this study, compared to a change of $9.0\ \mu M$ in the SCM induced by inspiratory threshold loading. These differences could be due to differences in FD versus CW processing and the assumptions related to the DPF, as well as differences in study procedures (i.e. duty cycle; intensity of MVC; isometric versus isotonic contractions; incremental versus constant load) and subject populations.

As shown in our results, sensitivity to SCM hemodynamics decreases as adipose thickness increases, likely leading to less accurate results for large (>5 mm) adipose thicknesses. Although substantial hemodynamic changes were observed in this study using an inverse model that assumes homogeneous tissue optical properties, going forward, a multilayer inverse model accounting for skin, subcutaneous adipose tissue, and muscle may improve sensitivity to the deeper SCM tissue. Parameters such as adipose thickness can be derived from ultrasound assessment of these tissues before application of the FD-NIRS optode. Additionally, some groups have now combined FD-NIRS with Diffuse Correlation Spectroscopy to calculate a blood flow index (BF_i) and muscle metabolic rate of oxygen (MRO_2) tissue metabolism, which provide a more complete picture of muscle metabolism [31,65,66]. SCM measurements would also likely benefit from this combination of techniques in future work.

5. Conclusion

We have shown that FD-NIRS is sensitive to hemodynamic changes in the SCM through both MC simulations and during quasi-isometric neck flexions of healthy volunteers. A custom digital FD-NIRS system was used to measure these changes. Based on these results, we hypothesize that FD-NIRS measurements of the SCM may provide an important new means to monitor patients during MV, potentially assisting with guiding appropriate unloading and weaning from MV.

Acknowledgments. The authors would like to thank BU's Electronics Design Facility for their help in designing and fabricating some of the custom electronics in the FD-NIRS system, and all of the healthy volunteers for their participation in the study.

Disclosures. None

Data availability. Data underlying the results presented in this paper are not publicly available at this time but may be obtained from the authors upon reasonable request.

Supplemental document. See Supplement 1 for supporting content.

References

1. H. Wunsch, W. T. Linde-Zwirble, D. C. Angus, M. E. Hartman, E. B. Milbrandt, and J. M. Kahn, "The epidemiology of mechanical ventilation use in the United States," Crit. Care Med. **38**(10), 1947–1953 (2010).
2. H. Wunsch, "Mechanical Ventilation in COVID-19: Interpreting the Current Epidemiology," Am. J. Respir. Crit. Care Med. **202**, 1 (2020).
3. A. B. Mehta, S. N. Syeda, R. S. Wiener, and A. J. Walkey, "Epidemiological trends in invasive mechanical ventilation in the United States: a population-based study," J. Crit. Care **30**(6), 1217–1221 (2015).
4. M. S. Herridge, L. M. Chu, A. Matte, G. Tomlinson, L. Chan, C. Thomas, J. O. Friedrich, S. Mehta, F. Lamontagne, M. Levasseur, N. D. Ferguson, N. K. J. Adhikari, J. C. Rudkowski, H. Meggison, Y. Skrobik, J. Flannery, M. Bayley, J. Batt, C. Dos Santos, S. E. Abbey, A. Tan, V. Lo, S. Mathur, M. Parotto, D. Morris, L. Flockhart, E. Fan, C. M. Lee, M. E. Wilcox, N. Ayas, K. Choong, R. Fowler, D. C. Scales, T. Sinuff, B. H. Cuthbertson, L. Rose, P. Robles, S. Burns, M. Cypel, L. Singer, C. Chaparro, C. W. Chow, S. Keshavjee, L. Brochard, P. Hebert, A. S. Slutsky, J. C. Marshall, D. Cook, and J. I. Cameron, "The RECOVER program: Disability risk groups and 1-year outcome after 7 or more days of mechanical ventilation," Am. J. Respir. Crit. Care Med. **194**(7), 831–844 (2016).
5. D. Adler, E. Dupuis-Lozeron, J. C. Richard, J. P. Janssens, and L. Brochard, "Does inspiratory muscle dysfunction predict readmission after intensive care unit discharge?" Am. J. Respir. Crit. Care Med. **190**, 347 (2014).
6. E. Damuth, J. A. Mitchell, J. L. Bartock, B. W. Roberts, and S. Trzeciak, "Long-term survival of critically ill patients treated with prolonged mechanical ventilation: A systematic review and meta-analysis," The Lancet Respiratory Medicine **3**(7), 544–553 (2015).
7. M. Dres and A. Demoule, "Diaphragm dysfunction during weaning from mechanical ventilation: an underestimated phenomenon with clinical implications," Critical Care **22**(1), 73 (2018).
8. M. Dres, B. P. Dube, J. Mayaux, J. Delemazure, D. Reuter, L. Brochard, T. Similowski, and A. Demoule, "Coexistence and impact of limb muscle and diaphragm weakness at time of liberation from mechanical ventilation in medical intensive care unit patients," Am. J. Respir. Crit. Care Med. **195**(1), 57–66 (2017).
9. M. Dres, B. P. Dubé, E. Goligher, S. Vorona, S. Demiri, E. Morawiec, J. Mayaux, L. Brochard, T. Similowski, and A. Demoule, "Usefulness of parasternal intercostal muscle ultrasound during weaning from mechanical ventilation," Anesthesiology **132**, 1114–1125 (2020).
10. A. W. Thille, I. Cortés-Puch, and A. Esteban, "Weaning from the ventilator and extubation in ICU," Current Opinion in Critical Care **19**(1), 57–64 (2013).
11. E. C. Goligher, L. J. Brochard, W. D. Reid, E. Fan, O. Saarela, A. S. Slutsky, B. P. Kavanagh, G. D. Rubenfeld, and N. D. Ferguson, "Diaphragmatic myotrauma: a mediator of prolonged ventilation and poor patient outcomes in acute respiratory failure," The Lancet Respiratory Medicine **7**(1), 90–98 (2019).
12. J. Batt, C. C. Dos Santos, J. I. Cameron, and M. S. Herridge, "Intensive care unit-acquired weakness clinical phenotypes and molecular mechanisms," Am. J. Respir. Crit. Care Med. **187**(3), 238–246 (2013).
13. M. Aubier, T. Trippenbach, and C. Roussos, "Respiratory muscle fatigue during cardiogenic shock," Journal of Applied Physiology **51**, 499–508 (1981).
14. S. Magder, "Bench-to-bedside review: ventilatory abnormalities in sepsis," Critical Care **13**, 202 (2009).
15. S. Parthasarathy, A. Jubran, F. Laghi, and M. J. Tobin, "Sternomastoid, rib cage, and expiratory muscle activity during weaning failure," J. Appl. Physiol. **103**, 140 (2007).
16. B. Shadgan, J. A. Guenette, A. W. Sheel, and W. D. Reid, "Sternocleidomastoid muscle deoxygenation in response to incremental inspiratory threshold loading measured by near infrared spectroscopy," Respiratory Physiology & Neurobiology **178**(2), 202–209 (2011).
17. N. Basoudan, B. Shadgan, J. A. Guenette, J. Road, and W. D. Reid, "Effect of acute hypoxia on inspiratory muscle oxygenation during incremental inspiratory loading in healthy adults," Eur. J. Appl. Physiol. **116**(4), 841–850 (2016).
18. T. Tanaka, N. Basoudan, L. T. Melo, L. Wickerson, L. J. Brochard, E. C. Goligher, and W. D. Reid, "Deoxygenation of inspiratory muscles during cycling, hyperpnoea and loaded breathing in health and disease: a systematic review," Clin. Physiol. Funct. Imaging **38**(4), 554–565 (2018).
19. A. Rodrigues, Z. Louvaris, S. Dacha, W. I. M. Janssens, F. Pitta, I. Vogiatzis, R. I. K. Gosselink, and D. Langer, "Differences in respiratory muscle responses to hyperpnea or loaded breathing in COPD," Med. Sci. Sports Exerc. **52**, 1126 (2020).
20. K. Katayama, Y. Suzuki, M. Hoshikawa, T. Ohya, M. Oriishi, Y. Itoh, and K. Ishida, "Hypoxia exaggerates inspiratory accessory muscle deoxygenation during hyperpnoea," Respiratory Physiology and Neurobiology **211**, 1–8 (2015).

21. P. B. Dominelli, B. Archiza, A. H. Ramsook, R. A. Mitchell, C. M. Peters, Y. Molgat-Seon, W. R. Henderson, M. S. Koehle, R. Boushel, and A. W. Sheel, "Effects of respiratory muscle work on respiratory and locomotor blood flow during exercise," Exp Physiol **102**(11), 1535–1547 (2017).

22. D. T. Delpy, M. Cope, P. Van Der Zee, S. Arridge, S. Wray, and J. Wyatt, "Estimation of optical pathlength through tissue from direct time of flight measurement," Physics in Medicine and Biology **33**, 1433 (1988).

23. I. J. Bigio and S. Fantini, *Quantitative Biomedical Optics* (Cambridge University Press, 2016).

24. L. F. Ferreira, D. M. Hueber, and T. J. Barstow, "Effects of assuming constant optical scattering on measurements of muscle oxygenation by near-infrared spectroscopy during exercise," J. Appl. Physiol. **102**(1), 358–367 (2007).

25. S. M. Hammer, D. M. Hueber, D. K. Townsend, L. M. Huckaby, A. M. Alexander, K. D. Didier, and T. J. Barstow, "Effect of assuming constant tissue scattering on measured tissue oxygenation values during tissue ischemia and vascular reperfusion," J. Appl. Physiol. **127**(1), 22–30 (2019).

26. T. H. Pham, O. Coquoz, J. B. Fishkin, E. Anderson, and B. J. Tromberg, "Broad bandwidth frequency domain instrument for quantitative tissue optical spectroscopy," Rev. Sci. Instrum. **71**(6), 2500–2513 (2000).

27. D. Roblyer, S. Ueda, A. Cerussi, W. Tanamai, A. Durkin, R. Mehta, D. Hsiang, J. A. Butler, C. McLaren, W.-P. Chen, and B. Tromberg, "Optical imaging of breast cancer oxyhemoglobin flare correlates with neoadjuvant chemotherapy response one day after starting treatment," Proc. Natl. Acad. Sci. **108**(35), 14626–14631 (2011).

28. A. Tank, H. M. Peterson, V. Pera, S. Tabassum, A. Leproux, T. O'Sullivan, E. Jones, H. Cabral, N. Ko, R. S. Mehta, B. J. Tromberg, and D. Roblyer, "Diffuse optical spectroscopic imaging reveals distinct early breast tumor hemodynamic responses to metronomic and maximum tolerated dose regimens," Breast Cancer Res. **22**(1), 29 (2020).

29. A. E. Cerussi, V. W. Tanamai, R. S. Mehta, D. Hsiang, J. Butler, and B. J. Tromberg, "Frequent optical imaging during breast cancer neoadjuvant chemotherapy reveals dynamic tumor physiology in an individual patient," Acad Radiol **17**(8), 1031–1039 (2010).

30. S. Fantini and A. Sassaroli, "Frequency-domain techniques for cerebral and functional near-infrared spectroscopy," Front. Neurosci. **14**, 1–18 (2020).

31. V. Quaresima, P. Farzam, P. Anderson, P. Y. Farzam, D. Wiese, S. A. Carp, M. Ferrari, and M. A. Franceschini, "Diffuse correlation spectroscopy and frequency-domain near-infrared spectroscopy for measuring microvascular blood flow in dynamically exercising human muscles," J. Appl. Physiol. **127**(5), 1328–1337 (2019).

32. M.-L. Chuang, I.-F. Lin, and M.-J. Hsieh, "More Impaired Dynamic Ventilatory Muscle Oxygenation in Congestive Heart Failure than in Chronic Obstructive Pulmonary Disease," J. Clin. Med. **8**(10), 1641 (2019).

33. Q. Fang and D. A. Boas, "Monte Carlo Simulation of Photon Migration in 3D Turbid Media Accelerated by Graphics Processing Units," Opt. Express **17**(22), 20178 (2009).

34. M. J. C. Van Gemert, S. L. Jacques, M. Sterenborg, and W. M. Star, "Skin Optics," 36, 1146–1154 (1989).

35. S. L. Jacques, "Erratum: Optical properties of biological tissues: a review," Physics in Medicine and Biology **58**(14), 5007–5008 (2013).

36. C. R. Simpson, M. Kohl, M. Essenpreis, and M. Cope, "Near-infrared optical properties of ex vivo human skin and subcutaneous tissues measured using the Monte Carlo inversion technique," Physics in Medicine and Biology **43**(9), 2465–2478 (1998).

37. J. Lai, Z. Li, C. Wang, and A. He, "Experimental measurement of the refractive index of biological tissues by total internal reflection," Appl. Opt. **44**(10), 1845–1849 (2005).

38. J. C. Lai, Y. Y. Zhang, Z. H. Li, H. J. Jiang, and A. Z. He, "Complex refractive index measurement of biological tissues by attenuated total reflection ellipsometry," Appl. Opt. **49**(16), 3235–3238 (2010).

39. A. N. Bashkatov, E. A. Genina, and V. V. Tuchin, "Optical properties of skin, subcutaneous, and muscle tissues: A review," J. Innovative Opt. Health Sci. **04**(01), 9–38 (2011).

40. A. N. Bashkatov, E. A. Genina, V. I. Kochubey, and V. V. Tuchin, "Optical properties of human skin, subcutaneous and mucous tissues in the wavelength range from 400 to 2000nm," J. Phys. D: Appl. Phys. **38**(15), 2543–2555 (2005).

41. I. Meglinski and A. Doronin, "Monte Carlo modeling of photon migration for the needs of biomedical optics and biophotonics," in *Advanced Biophotonics: Tissue Optical Sectioning* (Taylor and Francis, 2013), pp. 1–58.

42. G. Roggan, A. Dorschel, K. Minet, O. Wolff, and D. Muller, "The optical properties of biological tissue in the near infrared wavelength range–review and measurments," in *Laser-Induced Interstitial Thermotherapy, Institute Series*, I s13 (1995).

43. N. Bosschaart, G. J. Edelman, M. C. G. Aalders, T. G. Van Leeuwen, and D. J. Faber, "A literature review and novel theoretical approach on the optical properties of whole blood," Lasers Med. Sci. **29**(2), 453–479 (2014).

44. K. Chopra, D. Calva, M. Sosin, K. K. Tadisina, A. Banda, C. De La Cruz, M. R. Chaudhry, T. Legesse, C. B. Drachenberg, P. N. Manson, and M. R. Christy, "A comprehensive examination of topographic thickness of skin in the human face," Aesthetic Surgery Journal **35**(8), 1007–1013 (2015).

45. H.-J. Lee and J.-M. Song, "Deep neck flexor and sternocleidomastoid muscle thickness change in persons with no current neck pain using rehabilitative ultrasonograpic imaging," The Journal of Korean Physical Therapy **28**(6), 349–354 (2016).

46. B. S. Lin, C. W. Kong, D. C. Tarng, T. P. Huang, and G. J. Tang, "Anatomical variation of the internal jugular vein and its impact on temporary haemodialysis vascular access: An ultrasonographic survey in uraemic patients," Nephrology Dialysis Transplantation **13**(1), 134–138 (1998).

47. B. Grassi and V. Quaresima, "Near-infrared spectroscopy and skeletal muscle oxidative function in vivo in health and disease: a review from an exercise physiology perspective," J. Biomed. Opt. **21**(9), 091313 (2016).

48. W. G. Zijlstra, A. Buursma, and O. W. van Assendelft, *Visible and Near Infrared Absorption Spectra of Human and Animal Haemoglobin: Determination and Application* (Routledge, 2000).

49. G. Nishimura, I. Kida, and M. Tamura, "Characterization of optical parameters with a human forearm at the region from 1.15 to 1.52 μm using diffuse reflectance measurements," Physics in Medicine and Biology **51**(11), 2997–3011 (2006).

50. P. Ballard, D. E. Leahy, and M. Rowland, "Prediction of in vivo tissue distribution from in vitro data 1. Experiments with markers of aqueous spaces," Pharm. Res. **17**(6), 660–663 (2000).

51. L. Kou, D. Labrie, and P. Chylek, "Refractive indices of water and ice in the 065- to 25-μm spectral range," Appl. Opt. **32**(19), 3531 (1993).

52. J. Jung, R. Istfan, and D. Roblyer, "Note: A simple broad bandwidth undersampling frequency-domain digital diffuse optical spectroscopy system," Rev. Sci. Instrum. **85**(7), 076108 (2014).

53. A. Torjesen, R. Istfan, and D. Roblyer, "Ultrafast wavelength multiplexed broad bandwidth digital diffuse optical spectroscopy for in vivo extraction of tissue optical properties," J. Biomed. Opt. **22**(3), 036009 (2017).

54. Y. Zhao, M. B. Applegate, R. Istfan, A. Pande, and D. Roblyer, "Quantitative real-time pulse oximetry with ultrafast frequency-domain diffuse optics and deep neural network processing," Biomed. Opt. Express **9**(12), 5997 (2018).

55. M. B. Applegate and D. Roblyer, "Multi-distance diffuse optical spectroscopy with a single optode via hypotrochoidal scanning," Opt. Lett. **43**(4), 747 (2018).

56. A. Derbakova, S. Khuu, K. Ho, C. Lewis, T. Ma, L. T. Melo, K. F. Zabjek, E. C. Goligher, L. Brochard, G. Fregonezi, and W. D. Reid, "Neck and inspiratory muscle recruitment during inspiratory loading and neck flexion," *Medicine and Science in Sports and Exercise* (2020).

57. M. B. Applegate, C. A. Gómez, and D. Roblyer, "Modulation frequency selection and efficient look-up table inversion for frequency domain diffuse optical spectroscopy," J. of Biomedical Optics **26**, 1–15 (2021).

58. S. Fantini, M. A. Franceschini, and E. Gratton, "Semi-infinite-geometry boundary problem for light migration in highly scattering media: a frequency-domain study in the diffusion approximation," Journal of the Optical Society of America B **11**(10), 2128 (1994).

59. J. B. Fishkin and E. Gratton, "Propagation of photon-density waves in strongly scattering media containing an absorbing semi-infinite plane bounded by a straight edge," Journal of the Optical Society of America A **10**(1), 127 (1993).

60. C. K. Hayakawa, J. Spanier, F. Bevilacqua, A. K. Dunn, J. S. You, B. J. Tromberg, and V. Venugopalan, "Perturbation Monte Carlo methods to solve inverse photon migration problems in heterogeneous tissues," Opt. Lett. **26**, 1335 (2001).

61. I. Heinonen, S. Koga, K. K. Kalliokoski, T. I. Musch, and D. C. Poole, "Heterogeneity of muscle blood flow and metabolism: influence of exercise, aging, and disease states," Exercise and Sport Sciences Reviews **52**, 1610 (2015).

62. W. G. Murphy, "The sex difference in haemoglobin levels in adults - Mechanisms, causes, and consequences," Blood Rev. **28**(2), 41–47 (2014).

63. H. M. Peterson, A. Tank, D. S. Geller, R. Yang, R. Gorlick, B. H. Hoang, and D. Roblyer, "Characterization of bony anatomic regions in pediatric and adult healthy volunteers using diffuse optical spectroscopic imaging," J. Biomed. Opt. **25**(08), 1 (2020).

64. B. Chance, Q. Luo, S. Nioka, D. C. Alsop, and J. A. Detre, "Optical investigations of physiology: A study of intrinsic and extrinsic biomedical contrast," Philosophical Transactions of the Royal Society B: Biological Sciences **352**, 707 (1997).

65. S. A. Carp, P. Farzam, N. Redes, D. M. Hueber, and M. A. Franceschini, "Combined multi-distance frequency domain and diffuse correlation spectroscopy system with simultaneous data acquisition and real-time analysis," Biomed. Opt. Express **8**(9), 3993 (2017).

66. D. Tamborini, P. Farzam, B. Zimmermann, K.-C. Wu, D. A. Boas, and M. A. Franceschini, "Development and characterization of a multidistance and multiwavelength diffuse correlation spectroscopy system," Neurophotonics **5**(01), 1 (2018).